ACS Catalysis

Letter

pubs.acs.org/acscatalysis

High-Performance and Long-Lived Pd Nanocatalyst Directed by Shape Effect for CO Oxidative Coupling to Dimethyl Oxalate

Zhong-Ning Xu,[†,‡] Jing Sun,[†] Chen-Sheng Lin,[†] Xiao-Ming Jiang,[†] Qing-Song Chen,[†] Si-Yan Peng,[†] Ming-Sheng Wang,[†] and Guo-Cong Guo*[,†]

[†]State Key Laboratory of Structural Chemistry, Fujian Institute of Research on the Structure of Matter, Chinese Academy of Sciences, Fuzhou, Fujian 350002, P. R. China

[‡]Key Laboratory of Coal to Ethylene Glycol and Its Related Technology, Chinese Academy of Sciences, Fuzhou, Fujian 350002, P. R. China

Supporting Information

ABSTRACT: We synthesized monodisperse Pd nanocrystals with exposed (111) and (100) facets through preferentially oriented facet growth technology. We then supported them on α-Al_2O_3 as catalysts for application in CO oxidative coupling to dimethyl oxalate (DMO) and find, for the first time, that the (111) facets of Pd nanocrystals are active planes for CO oxidative coupling to DMO. This conclusion is based on experiment results, reaction mechanism, and density functional theory calculation. Directed by this shape effect, a high-performance and long-lived nanocatalyst with much lower Pd load for CO oxidative coupling to DMO was successfully prepared by a new wet impregnation−solution chemical reduction method, which can well control the exposure of (111) facets and sizes of Pd nanocrystals.

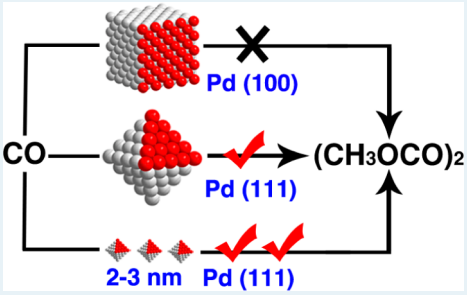

KEYWORDS: *CO oxidative coupling to dimethyl oxalate, Pd nanocatalyst, shape effect, wet impregnation−solution chemical reduction method*

CO oxidative coupling to dimethyl oxalate (DMO) plays a crucial role in many energy and environment-related processes, such as coal to ethylene glycol (CTEG), reuse of CO exhausts from factories, and so on. CTEG has attracted substantial attention because of its green and atomic economy (Figure S1 in Supporting Information (SI)),[1,2] which can greatly enhance the efficient and clean utilization of coal resources. The world's first set of 200 000 tons CTEG plant was built in 2009 (Figure S2 in the SI). CO oxidative coupling to DMO is the key step to realizing the conversion of inorganic C1 to organic C2 in CTEG.[3] In addition, lots of CO exhausts are emitted into the air from factories producing acetylene, phosphorus, steels, etc., which causes serious environmental pollution and resource waste. CO oxidative coupling to DMO can make full use of these CO exhausts to synthesize valuable chemicals and reduce environmental pollution.

Nano palladium-based heterogeneous catalysts have been demonstrated to be active for CO oxidative coupling to DMO.[4] The structure−reactivity relationship is one of the most essential issues in heterogeneous catalysis. The activity and selectivity of catalysts are strongly affected by both the size and shape of the nanocrystals in structure-sensitive reactions.[5−14] The quick developments in nanomaterials science provide a new opportunity to understand the origin of the structure−reactivity relationship by careful design and syntheses of size- and shape-controlled catalyst particles.[9,15−28,55]

Up to now, facet-dependent catalytic activities of noble metal anisotropic nanocrystals have been discovered in cross-coupling, electron transfer, hydrogenation, hydrogen evolution, the CO oxidation reaction, and electrocatalytic reactions.[29−37] For example, El-Sayed et al. have used Pt nanocrystals in the forms of cubes, spheres, and tetrahedra to catalyze the electron-transfer reaction between hexacyanoferrate and thiosulfate. They have interestingly observed that tetrahedral nanoparticles exposing mainly the (111) facets showed the highest activity, whereas cubic particles exposing the (100) facets exhibited the lowest activity.[38−40] Xia and co-workers found that (100)-facet-enclosed Pd nanocubes with slight truncations at the corners are the best catalysts for formic acid electrooxidation.[37] Yan et al. synthesized monodisperse single-crystalline sub-10 nm Pt−Pd nanotetrahedrons and nanocubes and used them as catalysts for methanol electrooxidation. Their results indicate that the (100)-facet-enclosed Pt−Pd nanocubes showed a higher activity, whereas the (111)-facet-bound Pt−Pd nanotetrahedrons held a better durability.[41] However, the correlation between the surface structure and catalytic performance of Pd nanocatalysts for CO oxidative coupling to DMO has been unknown so far. In addition, the reason for the facet-dependent catalytic activities was not further explored in most of the reports.

Although the solution chemical reduction method can well define the facets of metal nanocrystals for studying the

Received: May 6, 2012
Published: December 20, 2012

 © 2012 American Chemical Society

relationship between the catalytic activity and selectivity with the size and shape effects of metal nanocrystals, the model catalysts prepared by loading the metal nanocrystals on supports are unstable and more liable to change during catalytic reaction as a result of the weak interactions between the metal nanocrystals and supports.[42,43] On the other hand, the conventional wet-impregnation method could achieve stable catalysts, but cannot well control the facets and sizes of metal nanocrystals loaded on supports. Thus, development of an efficient preparation method that not only can well define the facets and sizes of metal nanocrystals but also obtain long-lived nanocatalysts is desirable.

Herein, we report for the first time that the (111) facets of Pd nanocrystals are active planes for CO oxidative coupling to DMO through evaluation of the catalytic activity of Pd nanocrystals supported on α-Al_2O_3 as catalysts as well as the reaction mechanism and density functional theory calculation. Meanwhile, on the basis of this finding, we have successfully synthesized a high-performance and long-lived supported Pd nanocatalyst with a much lower Pd load in comparison with the industrial catalyst by a new wet impregnation−solution chemical reduction method.

Monodisperse Pd nanopolyhedrons (NPHs) and nanocubes (NCs) were synthesized through preferentially oriented facet growth technology,[15] which is crucial for investigation of the effect of the facets on catalytic properties. Citric acid and formaldehyde were used as the capping agent and reductant, respectively, in the synthesis of Pd NPHs (see the experimental details in the SI), which ensured the as-synthesized Pd NPHs are mainly enclosed by (111) facets.[15,36,41,44] A TEM image of the as-synthesized Pd NPHs (Figure 1a) shows that the mean size of the Pd NPHs is 21.8 nm by the edge. The overwhelming majority of monodisperse Pd NPHs are octahedrons and truncated octahedrons, with only a few decahedrons and icosahedrons. A HRTEM image taken from an individual Pd truncated octahedron indicates that it is a single crystal with well-defined fringes (Figure 1b) and also suggests the high crystalline nature of the Pd NPHs. The lattice spacing along the edge of the octahedron is 0.228 nm, which is consistent with the (111) lattice spacing (0.226 nm) of the face-centered cubic (fcc) Pd, confirming that the as-synthesized Pd NPHs were mainly bounded by (111) planes, as confirmed by the corresponding fast Fourier transform (FFT) pattern viewed along the [110] zone axis (Figure 1b inset).

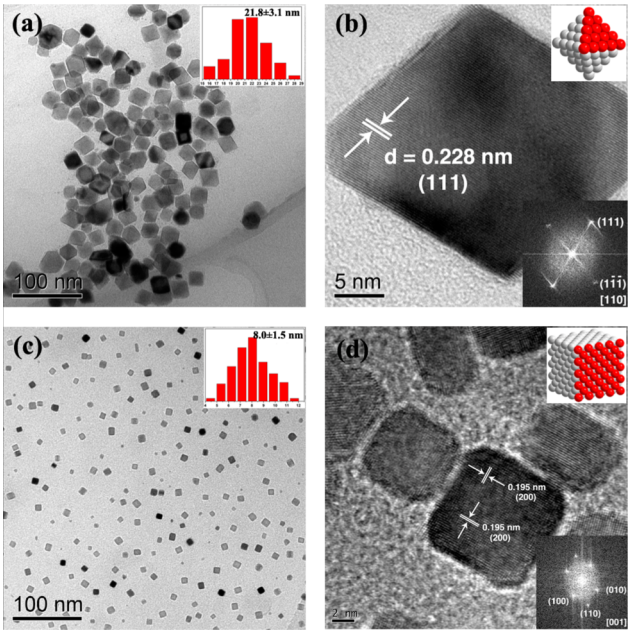

Figure 1. TEM images of Pd NPHs (a) and Pd NCs (c) and HRTEM images of Pd NPHs (b) and Pd NCs (d). The insets of panels a and c show the corresponding size distribution diagram. The insets of panels b and d show the corresponding FFT pattern and model.

Highly selective exposing (100) facets of Pd nanocrystals was obtained with the aid of the Br^- ion (see the experimental details in the SI).[15,45] A TEM image of as-synthesized monodisperse Pd NCs with almost 100% selectivity and a mean width size of 8 nm is shown in Figure 1c. A HRTEM image of several NCs shows that the as-synthesized Pd NCs are well-faceted single crystals (Figure 1d). The intervals between two lattice fringes along the two edges of a cube shown in the HRTEM image are 0.195 nm, close to that of the (200) lattice spacing (0.197 nm) of fcc Pd, as indicated by the FFT pattern along the [001] zone axis (Figure 1d inset), which demonstrates that the exposed facets of the as-synthesized Pd NCs are (100) facets. The enhanced relative intensity of the (200) peak to the (111) peak in the XRD pattern of Pd NCs (Figure S4b in the SI) (as compared with Pd NPHs) further confirmed that the Pd NCs were surrounded by (100) facets.

The Pd NPH/α-Al_2O_3 catalyst (**1**) and Pd NC/α-Al_2O_3 catalyst (**2**) were prepared by well dispersing the as-synthesized monodisperse Pd NPHs and NCs on the α-Al_2O_3 support surface and were characterized by XRD and TEM (Figures S5 and S6 in the SI), showing that the Pd nanocrystals remain unchanged during the supporting process. An XPS spectrum of catalyst **2** (Figure S10 in the SI) has demonstrated no bromides remained on the surface of Pd NCs, which can rule out the effect of bromide ions on the catalytic activity of Pd NCs in our experiments.

In comparison with the industrial catalyst, the catalytic activities of catalysts **1** and **2** for CO oxidative coupling to DMO were evaluated under the same reaction conditions (Table 1, Table S1 in the SI). Both the space−time yield (STY) of DMO and the TOF value of catalyst **1** are much higher than those of catalyst **2**, which demonstrates that the (111) facets of Pd nanocrystals are a benefit for CO oxidative coupling to DMO.

Table 1. CO Oxidative Coupling to DMO on Different Catalysts[a]

catalysts	STY[b] of DMO [g L^{-1} h^{-1}]	TOF[c] (s^{-1})
1	642	1.2
2	79	0.04

[a]Reaction conditions: 200 mg of catalyst, 3000 h^{-1} of gas hourly space velocity (GHSV), 0.1 MPa, 130 °C (see more details in the SI). [b]STY represents the space−time yield, grams of product per liter of catalyst per hour (g L^{-1} h^{-1}). [c]TOF represents turnover frequently (see more calculation details in the SI).

Pd 3d XPS spectra of fresh catalysts **1** and **2**, catalysts **1A** and **2A** from catalysts **1** and **2** treated with methyl nitrite, and catalysts **1B** and **2B** from catalysts **1** and **2** treated with methyl nitrite and CO at 130 °C were tested (Figure 2). Both the Pd $3d_{5/2}$ and Pd $3d_{3/2}$ of catalysts **1** and **2** are at 335 and 340 eV, respectively, showing the oxidation state of Pd in catalysts **1** and **2** is Pd(0).[46] Two new peaks appeared at 337 and 342 eV

dx.doi.org/10.1021/cs300759h | ACS Catal. 2013, 3, 118−122

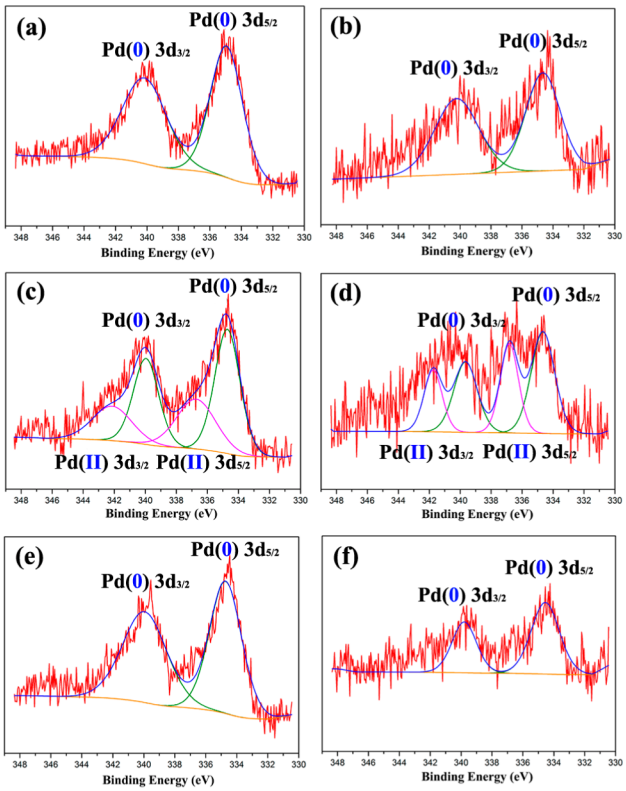

Figure 2. Pd 3d XPS spectra of catalysts **1** and **2** (a and b), catalysts **1A** and **2A** (c and d), and catalysts **1B** and **2B** (e and f), respectively.

in catalysts **1A** and **2A**, which are assigned to Pd(II),[46] indicating that some Pd(0) in catalysts **1** and **2** was oxidized to Pd(II) by methyl nitrite to form an intermediate, $CH_3O-Pd(II)-OCH_3$ (**1**), and NO. The in situ diffuse reflectance infrared (DRIR) spectra of CO on both catalysts, **1** and **2**, at 130 °C (Figure S11a and b in the SI) show that the adsorption mode of CO on the Pd nanocrystals in catalysts **1** and **2** is mainly linear, indicating that the linearly adsorbed CO inserts into the intermediate **1** to form another intermediate, $CH_3OCO-Pd(II)-COOCH_3$ (**2**).[47] The intermediate **2** quickly occurs in the intramolecular coupling elimination reaction, resulting in the formation of DMO and the reduction of Pd(II) to Pd(0), according to the Pd(0) state in catalysts **1B** and **2B**. Therefore, the catalytic mechanism of CO oxidative coupling to DMO can be reasonably proposed as shown in Figure 3.

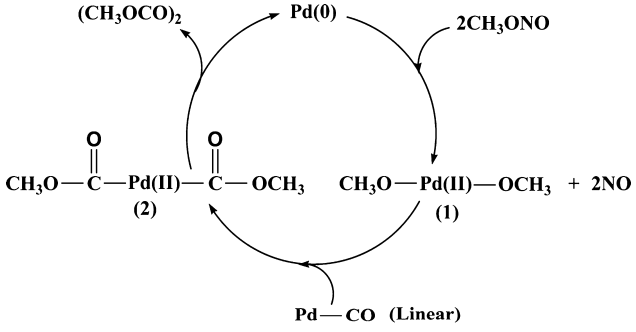

Figure 3. The proposed catalytic mechanism of CO oxidative coupling to DMO.

It is worth noting that a new band at 1770 cm^{-1} in the in situ DRIR spectrum of the reaction of CO and methyl nitrite to DMO, which is ascribed to the C═O stretching vibrations of DMO, or intermediate **2**, emerges for catalyst **1** (Figure 4a) but

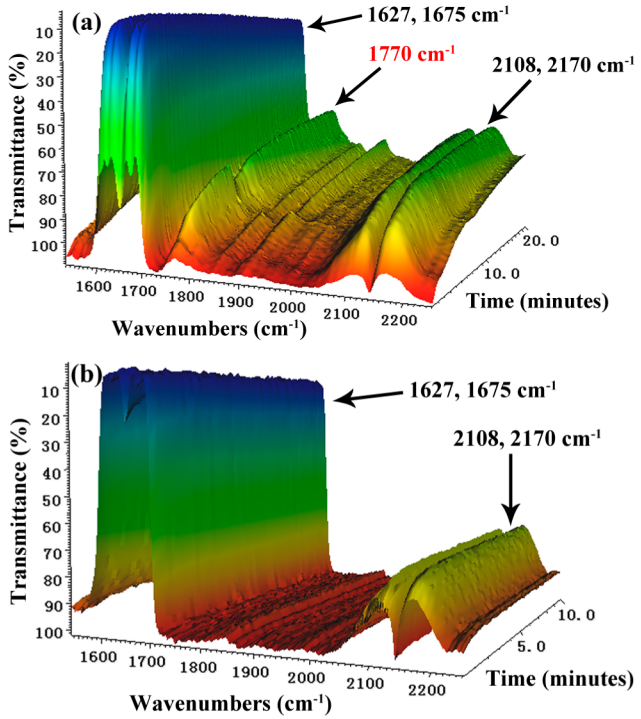

Figure 4. The in situ DRIR spectra of the reaction of CO and methyl nitrite to DMO on catalysts **1** and **2** (a and b) at 130 °C, respectively.

not for catalyst **2** (Figure 4b), demonstrating the superior catalytic activity of the (111) facets of Pd nanocrystals relative to the (100) facets, which is consistent with the result mentioned above. Moreover, the new band at 1770 cm^{-1} exists for catalyst **1**, but does fails to appear for catalyst **2** over the whole time range. The bands at 1627 and 1675 cm^{-1} are ascribed to the N═O vibrations of methyl nitrite, and the bands at 2108 and 2170 cm^{-1} are assigned to CO in the gaseous state.

The charge distribution and binding energy of CO adsorbed on (111) and (100) facets of Pd by different adsorption models (Table 2) were calculated by density functional theory (DFT)[48−53] in the plane-wave-based Vienna ab initio simulation package (VASP), respectively. The positive charges of the C atom for CO adsorbed on Pd decrease in the order of linear > bridge > hollow, and the binding energies increase in

Table 2. The Charge Distribution and Binding Energy of CO Adsorbed on (111) and (100) Facets of Pd by Different Adsorption Models

absorption models	Bader charge, C	binding energy, (eV)
(100) linear	0.9016	−1.4533
(100) bridge	0.8030	−1.9915
(100) hollow	0.5766	−1.8185
(111) linear	0.9547	−1.0281
(111) bridge	0.7940	−1.4516
(111) hollow (hcp)	0.7061	−1.6343
(111) hollow (fcc)	0.7547	−1.6513

dx.doi.org/10.1021/cs300759h | ACS Catal. 2013, 3, 118−122

the order of linear < bridge < hollow (minus sign means the CO adsorption is an exothermal process), which are coincident with those reported by Freund.[52] Generally, the higher the positive charge of the C atom implies the CO adsorbed on the surface of Pd prefers electrophilic insertion into a methoxy group with a part negative charge. On the other hand, the lower binding energy implies CO can easily move on the surface of Pd for the electrophilic insertion reaction. It is interesting to note that the positive charges of the C atom for CO linearly adsorbed on (111) facets of Pd are significantly larger in comparison with (100) facets of Pd, whereas the binding energies are just the opposite. Accordingly, on the basis of experiment results, reaction mechanism, and calculation, the linear absorption mode of CO and the Pd (111) facets are crucial to CO oxidative coupling to DMO.

Although the preparation method of catalysts **1** and **2** can well define the facets of Pd nanocrystals for the study on the relationship between the catalytic activity and selectivity with the size and shape effect of catalysts, the model catalysts are unstable and more liable to change during catalytic reaction due to the weak interactions between the Pd nanocrystals and the Al_2O_3 support. To overcome this problem, we have developed a new wet impregnation−solution chemical reduction method and successfully prepared a Pd NP/α-Al_2O_3 catalyst (**3**) with higher catalytic performance and lower Pd load in comparison with the industrial catalyst.

A TEM image of catalyst **3** shows that the Pd NPs are highly and evenly supported on the α-Al_2O_3 surface, with an average size of 2.4 nm (Figure 5a). A HRTEM image of catalyst **3**

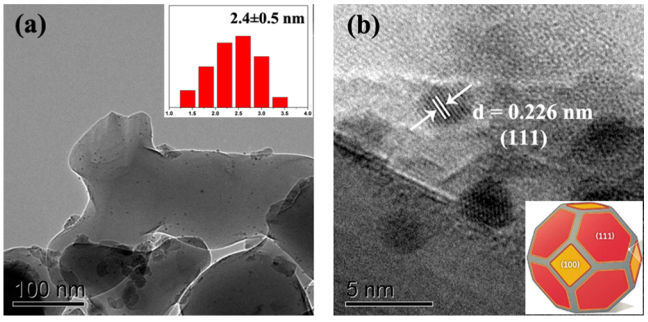

Figure 5. TEM (a) and HRTEM (b) images of catalyst **3**. The inset of panel a shows the size distribution diagram. The inset of panel b shows a model of cuboctahedron.

reveals that the interval between two lattice fringes of Pd NPs is 0.226 nm (Figure 5b), indicating that the small Pd NPs are single crystals. Electrochemical methods (cyclic voltammograms and CO stripping) were carried out to investigate the mainly exposed planes of small Pd NPs. Both the blank cyclic voltammogram and CO stripping character of catalyst **3** in 0.1 M $HClO_4$ are very similar to those of Pd NPHs (Figure S9 in SI), indicating the surface of Pd NPs is dominated by (111) domains. It is coincident with common knowledge that small NPs are predominated by cuboctahedrons mainly enclosed by (111) facets (Figure 5b inset).[54] The actual Pd load is only 0.37% measured by ICP, which is too low to show any diffraction peaks of Pd in the XRD pattern of catalyst **3** (Figure S5c in the SI).

The catalytic performances of catalyst **3** were evaluated under the same conditions as the industrial catalyst. The STY of DMO of catalyst **3** increases greatly with an increase in the reaction temperature, which is 40% higher than that of industrial catalyst with 2% of Pd load at 130 °C (Figure 6a).

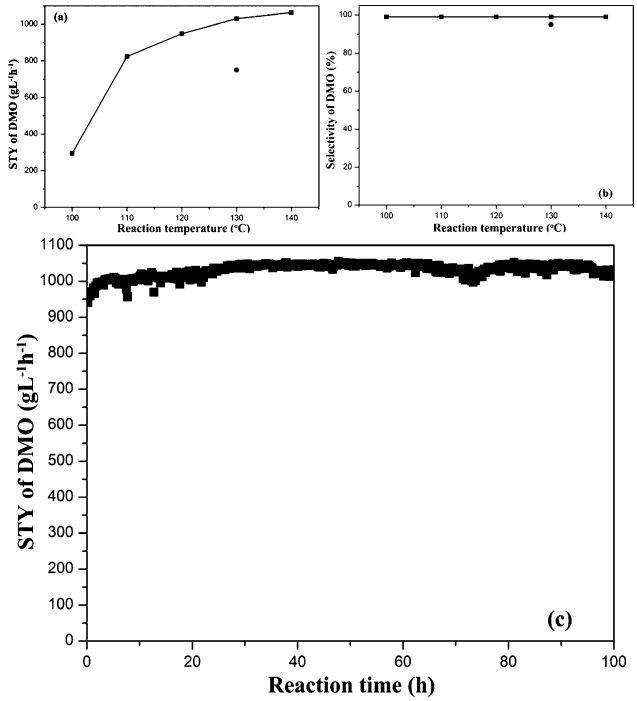

Figure 6. STY of DMO (a) and selectivity of DMO (b) of catalyst **3** (■) and industrial catalyst (●) for CO oxidative coupling to DMO at different reaction temperatures. STY of DMO (c) of catalyst **3** at 130 °C for 100 h.

Meanwhile, the selectivity of DMO of catalyst **3** is close to 100% and is constant in the range 100−140 °C, which is also superior in comparison with the industrial catalyst (Figure 6b). Consequently, the exposed (111) facets of Pd nanocrystals are responsible for the high activity and selectivity in CO oxidative coupling to DMO. Most of all, the catalytic activity of catalyst **3** can be maintained for at least 100 h, which lays a good foundation for further enlarging a long-term stability test (Figure 6c). The TEM image of catalyst **3** after 100 h evaluation shows that the Pd NPs are also well dispersed on the α-Al_2O_3 surface and have not agglomerated during the catalytic process (Figure S7 in the SI), which further demonstrates that the new method is very useful for preparing practical nanocatalysts.

In summary, the experiment results, reaction mechanism, and density functional theory calculation have demonstrated that the exposed (111) facets of Pd nanocatalysts are active planes for CO oxidative coupling to DMO. The new wet impregnation−solution chemical reduction method is quite useful for controlling the exposure of the (111) facets and sizes of Pd nanocrystals supported on α-Al_2O_3 as a high-performance and long-lived nanocatalyst with much lower Pd load for CO oxidative coupling to DMO. This work provides new insights for rationally designing new higher-performance nanocatalysts for CO oxidative coupling to DMO and greatly reducing the precious metal load.

■ ASSOCIATED CONTENT

Ⓢ Supporting Information

Reactions of coal to ethylene glycol, photo of coal to ethylene glycol plant, experimental details, XRD patterns, TEM images,

dx.doi.org/10.1021/cs300759h | ACS Catal. 2013, 3, 118−122

cyclic voltammograms, CO stripping, XPS spectra and CO in situ DRIR spectra of catalysts, conversion of CO, TOF values of catalysts, and GC chromatogram of the products on catalysts. This material is available free of charge via the Internet at http://pubs.acs.org.

AUTHOR INFORMATION

Corresponding Author

*E-mail: gcguo@fjirsm.ac.cn.

Notes

The authors declare no competing financial interest.

ACKNOWLEDGMENTS

We gratefully acknowledge financial support from the 973 Program (2011CBA00505), National Key Technology R&D Program (2012BAE06B08), NSF of China (90922035, 21003126), Key Project from the CAS (KJCX2.YW.M10), and the NSF of Fujian province.

REFERENCES

(1) Li, X. Z.; Chen, Y.; Chen, J. Q. *Coal Chem. Ind.* **2007**, 15−18.
(2) Zhou, Z. F.; Li, Z. J.; Pan, P. B.; Lin, L.; Qin, Y. Y.; Yao, Y. G. *Chem. Ind. Eng. Prog.* **2010**, *29*, 2003−2009.
(3) Fenton, D. M.; Steinwan, P. J. *J. Org. Chem.* **1974**, *39*, 701−704.
(4) Yamamoto, Y. *Catal. Surv. Asia* **2010**, *14*, 103−110.
(5) Somorjai, G. A. *Appl. Surf. Sci.* **1997**, *121*, 1−19.
(6) Somorjai, G. A.; Li, Y. M. *Top. Catal.* **2010**, *53*, 832−847.
(7) Lee, H.; Habas, S. E.; Kweskin, S.; Butcher, D.; Somorjai, G. A.; Yang, P. D. *Angew. Chem., Int. Ed.* **2006**, *45*, 7824−7828.
(8) Crespo-Quesada, M.; Yarulin, A.; Jin, M. S.; Xia, Y. N.; Kiwi-Minsker, L. *J. Am. Chem. Soc.* **2011**, *133*, 12787−12794.
(9) Xia, Y. N.; Xiong, Y. J.; Lim, B.; Skrabalak, S. E. *Angew. Chem., Int. Ed.* **2009**, *48*, 60−103.
(10) Narayanan, R.; El-Sayed, M. A. *J. Phys. Chem. B* **2005**, *109*, 12663−12676.
(11) van Santen, R. A.; Neurock, M.; Shetty, S. G. *Chem. Rev.* **2010**, *110*, 2005−2048.
(12) Semagina, N.; Kiwi-Minsker, L. *Catal. Rev. Sci. Eng.* **2009**, *51*, 147−217.
(13) Zaera, F. *Acc. Chem. Res.* **2009**, *42*, 1152−1160.
(14) Li, Y.; Liu, Q. Y.; Shen, W. J. *Dalton Trans.* **2011**, *40*, 5811−5826.
(15) Lim, B.; Jiang, M. J.; Tao, J.; Camargo, P. H. C.; Zhu, Y. M.; Xia, Y. N. *Adv. Funct. Mater.* **2009**, *19*, 189−200.
(16) Lim, B.; Xia, Y. N. *Angew. Chem., Int. Ed.* **2011**, *50*, 76−85.
(17) Xiong, Y. J.; Xia, Y. N. *Adv. Mater.* **2007**, *19*, 3385−3391.
(18) Wang, X.; Peng, Q.; Li, Y. D. *Acc. Chem. Res.* **2007**, *40*, 635−643.
(19) Wang, D. S.; Li, Y. D. *Adv. Mater.* **2011**, *23*, 1044−1060.
(20) Wang, D. S.; Xie, T.; Li, Y. D. *Nano Res.* **2009**, *2*, 30−46.
(21) Sau, T. K.; Rogach, A. L. *Adv. Mater.* **2010**, *22*, 1781−1804.
(22) Zhang, L.; Zhang, J. W.; Kuang, Q.; Xie, S. F.; Jiang, Z. Y.; Xie, Z. X.; Zheng, L. S. *J. Am. Chem. Soc.* **2011**, *133*, 17114−17117.
(23) Huang, X. Q.; Zhao, Z. P.; Fan, J. M.; Tan, Y. M.; Zheng, N. F. *J. Am. Chem. Soc.* **2011**, *133*, 4718−4721.
(24) Huang, X. Q.; Tang, S. H.; Yang, J.; Tan, Y. M.; Zheng, N. F. *J. Am. Chem. Soc.* **2011**, *133*, 15946−15949.
(25) Huang, X. Q.; Tang, S. H.; Mu, X. L.; Dai, Y.; Chen, G. X.; Zhou, Z. Y.; Ruan, F. X.; Yang, Z. L.; Zheng, N. F. *Nat. Nanotechnol.* **2011**, *6*, 28−32.
(26) Huang, X. Q.; Tang, S. H.; Zhang, H. H.; Zhou, Z. Y.; Zheng, N. F. *J. Am. Chem. Soc.* **2009**, *131*, 13916−13917.
(27) Huang, X. Q.; Zhang, H. H.; Guo, C. Y.; Zhou, Z. Y.; Zheng, N. F. *Angew. Chem., Int. Ed.* **2009**, *48*, 4808−4812.
(28) Huang, X. Q.; Zheng, N. F. *J. Am. Chem. Soc.* **2009**, *131*, 4602−4603.
(29) Bing, Y. H.; Liu, H. S.; Zhang, L.; Ghosh, D.; Zhang, J. J. *Chem. Soc. Rev.* **2010**, *39*, 2184−2202.
(30) Subhramannia, M.; Pillai, V. K. *J. Mater. Chem.* **2008**, *18*, 5858−5870.
(31) Tian, N.; Zhou, Z. Y.; Sun, S. G. *J. Phys. Chem. C* **2008**, *112*, 19801−19817.
(32) Chen, J. Y.; Lim, B.; Lee, E. P.; Xia, Y. N. *Nano Today* **2009**, *4*, 81−95.
(33) Jia, C. J.; Schuth, F. *Phys. Chem. Chem. Phys.* **2011**, *13*, 2457−2487.
(34) Kotani, H.; Hanazaki, R.; Ohkubo, K.; Yamada, Y.; Fukuzumi, S. *Chem.−Eur. J.* **2011**, *17*, 2777−2785.
(35) Tsung, C. K.; Kuhn, J. N.; Huang, W. Y.; Aliaga, C.; Hung, L. I.; Somorjai, G. A.; Yang, P. D. *J. Am. Chem. Soc.* **2009**, *131*, 5816−5822.
(36) Jin, M.; Zhang, H.; Xie, Z.; Xia, Y. *Energy Environ. Sci.* **2012**, 6352−6357.
(37) Wang, R.; He, H.; Liu, L.-C.; Dai, H.-X.; Zhao, Z. *Catal. Sci. Technol.* **2012**, *2*, 575−580.
(38) Narayanan, R.; El-Sayed, M. A. *J. Am. Chem. Soc.* **2004**, *126*, 7194−7195.
(39) Narayanan, R.; El-Sayed, M. A. *J. Phys. Chem. B* **2004**, *108*, 5726−5733.
(40) Narayanan, R.; El-Sayed, M. A. *Nano Lett.* **2004**, *4*, 1343−1348.
(41) Yin, A. X.; Min, X. Q.; Zhang, Y. W.; Yan, C. H. *J. Am. Chem. Soc.* **2011**, *133*, 3816−3819.
(42) Narayanan, R.; El-Sayed, M. A. *J. Am. Chem. Soc.* **2004**, *126*, 7194−7195.
(43) Zhou, K. B.; Li, Y. D. *Angew. Chem., Int. Ed.* **2012**, *51*, 602−613.
(44) Yin, A. X.; Min, X. Q.; Zhu, W.; Wu, H. S.; Zhang, Y. W.; Yan, C. H. *Chem. Commun.* **2012**, *48*, 543−545.
(45) Jin, M. S.; Liu, H. Y.; Zhang, H.; Xie, Z. X.; Liu, J. Y.; Xia, Y. N. *Nano Res.* **2011**, *4*, 83−91.
(46) Chen, Y. T.; Guo, Z.; Chen, T.; Yang, Y. H. *J. Catal.* **2010**, *275*, 11−24.
(47) Gao, Z. H.; Liu, Z. C.; He, F.; Xu, G. H. *J. Mol. Catal. A: Chem.* **2005**, *235*, 143−149.
(48) Tüshaus, M.; Berndt, W.; Conrad, H.; Bradshaw, A. M.; Persson, B. *Appl. Phys. A: Mater. Sci. Process.* **1990**, *51*, 91−98.
(49) Loffreda, D.; Simon, D.; Sautet, P. *Surf. Sci.* **1999**, *425*, 68−80.
(50) Sautet, P.; Rose, M. K.; Dunphy, J. C.; Behler, S.; Salmeron, M. *Surf. Sci.* **2000**, *453*, 25−31.
(51) Rose, M. K.; Mitsui, T.; Dunphy, J.; Borg, A.; Ogletree, D. F.; Salmeron, M.; Sautet, P. *Surf. Sci.* **2002**, *512*, 48−60.
(52) Yudanov, I. V.; Sahnoun, R.; Neyman, K. M.; Rösch, N.; Hoffmann, J.; Schauermann, S.; Johánek, V.; Unterhalt, H.; Rupprechter, G.; Libuda, J.; Freund, H.-J. *J. Phys. Chem. B* **2002**, *107*, 255−264.
(53) Zhang, C. J.; Hu, P. *J. Am. Chem. Soc.* **2001**, *123*, 1166−1172.
(54) Poltorak, O. M.; Boponi, B. S. *J. Phys. Chem.* **1966**, *40*, 1436.
(55) Zhang, H.; Jin, M.; Xiong, Y.; Lim, B.; Xia, Y. *Acc. Chem. Res.* **2012**, DOI: 10.1021/ar300209w.